Stable Universal 1- and 2-Input Single-Molecule Logic Gates

Ran Liu, Yingmei Han, Feng Sun, Gyan Khatri, Jaesuk Kwon, Cameron Nickle, Lejia Wang, Chuan-Kui Wang, Damien Thompson, Zong-Liang Li,* Christian A. Nijhuis,* and Enrique del Barco*

Controllable single-molecule logic operations will enable development of reliable ultra-minimalistic circuit elements for high-density computing but require stable currents from multiple orthogonal inputs in molecular junctions. Utilizing the two unique adjacent conductive molecular orbitals (MOs) of gated Au/S-$(CH_2)_3$-Fc-$(CH_2)_9$-S/Au (Fc = ferrocene) single-electron transistors (≈2 nm), a stable single-electron logic calculator (SELC) is presented, which allows real-time modulation of output current as a function of orthogonal input bias (V_b) and gate (V_g) voltages. Reliable and low-voltage ($|V_b| \leq 80$ mV, $|V_g| \leq 2$ V) operations of the SELC depend upon the unambiguous association of current resonances with energy shifts of the MOs (which show an invariable, small energy separation of ≈100 meV) in response to the changes of voltages, which is confirmed by electron-transport calculations. Stable multi-logic operations based on the SELC modulated current conversions between the two resonances and Coulomb blockade regimes are demonstrated via the implementation of all universal 1-input (YES/NOT/PASS_1/PASS_0) and 2-input (AND/XOR/OR/NAND/NOR/INT/XNOR) logic gates.

1. Introduction

Effective control of electronic properties of molecular junctions for stable rectification,[1–2] switching,[3–4] memory,[5–6] and logic operation[7–12] is critical for reducing the area and power consumption of electrical circuits. Important advances have been made in the design of multifunctional molecular devices that employ external stimuli (e.g., chemical, light, magnetic, or electric field) to modulate electron transport through molecular junctions.[2,3,5,7,11,13–21] The modulations typically rely on stimulus-induced changes in molecular electronic states[5,14,22] and therefore the functional diversity and signal stability of molecular devices depend on the availability of different stable electronic states and efficient conversions between them.[2,3,7,23] As all-electrical-driven devices, three-terminal solid-state single-electron transistors (SETs)[17,24–30] not only reflect the quantum behavior of intramolecular electron transport, such as Coulomb blockade,[19,20,31,32] Zeeman effect,[20,21] thermoelectric properties[25,26,33] and Kondo effect,[21,34–36] but also have the unique advantage of controlling the molecular orbitals (MOs) by applying external electrostatic potentials,[17,26,36–39] thereby providing new opportunities for the ultra-miniaturization of computing elements.[40–43] However, there are still two key challenges in utilizing SETs in single-molecule functional devices. First, the background electrostatic potentials of molecular junctions that affect the absolute energy of MOs are difficult to control, and so the resonance regions determined by MOs are normally different for different junctions formed with the same

R. Liu, G. Khatri, J. Kwon, C. Nickle, E. del Barco
Department of Physics
University of Central Florida
Orlando, FL 32816, USA
E-mail: delbarco@ucf.edu

Y. Han, L. Wang, C. A. Nijhuis
Department of Chemistry
National University of Singapore
3 Science Drive 3, Singapore 117543, Singapore

F. Sun, C.-K. Wang, Z.-L. Li
Key Laboratory of Medical Physics and Image Processing
of Shandong Province
School of Physics and Electronics
Shandong Normal University
Jinan 250358, P. R. China
E-mail: lizongliang@sdnu.edu.cn

L. Wang
School of Materials and Chemical Engineering
Ningbo University of Technology
Ningbo 315048, P. R. China

D. Thompson
Department of Physics
Bernal Institute
University of Limerick
Limerick V94 T9PX, Ireland

C. A. Nijhuis
Hybrid Materials for Opto-Electronics Group
Department of Molecules and Materials
MESA+ Institute for Nanotechnology
Molecules Center and Center for Brain-Inspired Nano Systems
Faculty of Science and Technology
University of Twente
Enschede 7500 AE, Netherlands
E-mail: c.a.nijhuis@utwente.nl

ADVANCED
SCIENCE NEWS
www.advancedsciencenews.com

ADVANCED
MATERIALS
www.advmat.de

molecule.[19,20,31,43] Second, the multifunctional implementation requires clear boundaries between Coulomb blockade and resonance regimes,[20,28,32] which are complicated by the electrode-induced energy-level broadening of MOs.[17,28,29,44]

Targeting these two challenges, we screened Au/S-$(CH_2)_3$-Fc-$(CH_2)_9$-S/Au (Fc = ferrocene) SETs from five different kinds of Fc-based gated SET junctions (see Figure 3 and Figure S14, Supporting Information) and designed a prototype single-electron logic calculator (SELC). First, instead of relying on absolute currents affected by the uncertainty of background electrostatic potentials, we employ current conversions between two sturdy and well-defined resonance regimes rendered by two adjacent conductive MOs of Fc. The MOs have a stable, small energy separation of around 100 meV and sit close to the Fermi energy of the electrodes in all five different Fc-based SETs and our DFT calculations show that this energy signature is not dependent on the conformation of the molecule inside the transistor.[24,25,45–48] Crucially, our measurements and calculations show that the current conversions due to the modulation of MOs by gate (V_g) and bias (V_b) voltages are stable. Second, we used n-alkyl ($-(CH_2)_n-$, $n \geq 3$) linkers to weaken the coupling between the molecule and the electrodes, that is, to minimize the broadening of the MO energy levels[25] on the Fc moiety by effectively isolating Fc from the electrodes.[16,49,50] Hence, we obtained a sharp-edged diamond-shaped Coulomb blockade regime in Au/S-$(CH_2)_3$-Fc-$(CH_2)_9$-S/Au SETs that allows the generation of clear current switching signals. The small energy separation of the two adjacent conductive MOs of Fc supports logic operations at low input voltages ($|V_b| \leq 80$ mV, $|V_g| \leq 2$ V)

far below the 1.5–5 V drive voltage and 3–15 V gate voltage of complementary metal–oxide–semiconductor (CMOS). By implementing all universal logic gates (the four 1-input gates YES, NOT, PASS_1, and PASS_0 and the seven 2-input gates AND, XOR, OR, NAND, NOR, INT, and XNOR), we demonstrate reliable programmable logic operations based on one single-molecule SET.

2. The SELC Design

Figure 1A,B shows the schematic configuration and circuit design of the three-terminal SELC comprising the functional Au/S-$(CH_2)_3$-Fc-$(CH_2)_9$-S/Au molecular junction (see Sections S1 and S2, Supporting Information, for details) strung over an Al back-gate (third terminal) with Al_2O_3 as the insulating layer between the junction and the gate. Along the junction, the Fc moiety is electronically isolated by the $-(CH_2)_3-$ and $-(CH_2)_9-$ linkers on either side and the molecule is connected to the source and drain nano-electrodes by thiolate–metal bonds. Studies of similar Fc-based molecules in three-terminal SETs[24,25] and SAM-based junctions[49,51–53] have shown that asymmetric $-(CH_2)_n-$ linkers cause unequal coupling between the molecule and the electrodes, leading to current rectification[49] and thus providing a natural route to encode information via orthogonal modulations of the MOs by V_g and V_b. To minimize the probability of several molecules bridging one nanogap, we created low coverage of molecules on an array of gold electrodes[21] (see Section S2, Supporting Information). In
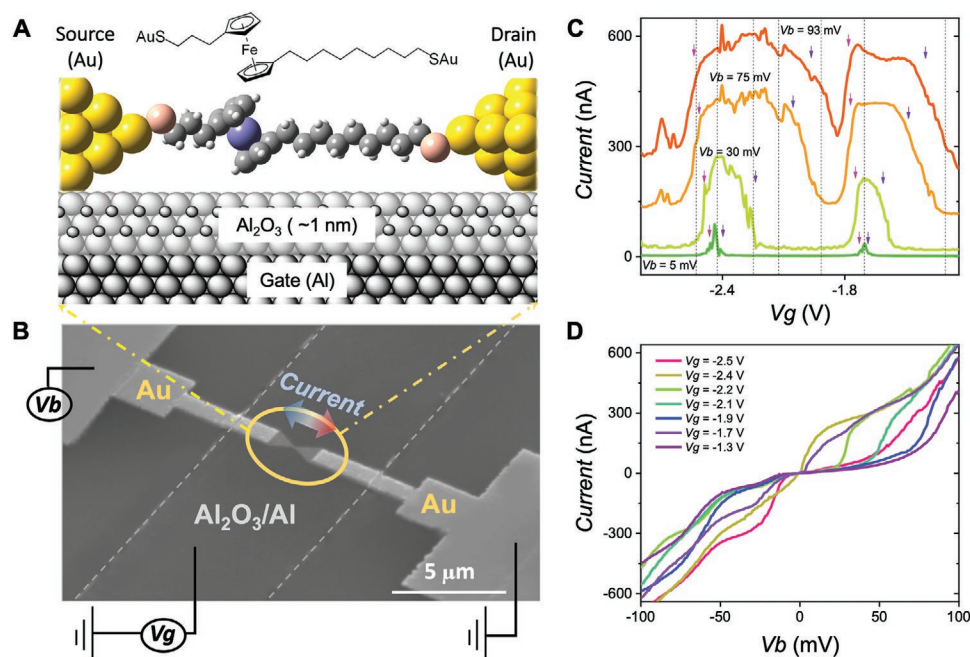

Figure 1. The design of SELC. A) Chemical structure and schematic of an S-$(CH_2)_3$-Fc-$(CH_2)_9$-S molecule bridging the nanogap between two nano-electrodes. B) SEM image of a SELC showing the Au nanowire on the Al_2O_3/Al back-gate on a Si wafer and positions where V_b and V_g are applied. The nanowire and the back-gate are patterned by electron-beam and optical lithography, respectively.[54] The molecular junction formed in the center of the nanowire is produced using current feedback-controlled electromigration[17,25,55,56] (see Section S2, Supporting Information, for details). C) Representative I–V_g curves for different values of V_b measured at 225 mK with 231 points per curve. The arrows mark the switch points of the current plateaus. The dashed lines indicate the V_g values corresponding to the seven I–V_b curves in (D). D) Representative I–V_b curves for the seven different V_g values, with 231 points per curve. $T = 225$ mK.

**ADVANCED
SCIENCE NEWS**

www.advancedsciencenews.com

**ADVANCED
MATERIALS**

www.advmat.de

the experiment, after electromigration, 37 of the 214 correctly broken nanowires showed a molecular signal (current of nA scale, see Figure S3, Supporting Information) different from a bare tunneling. That is, less than 20% of the nanogaps could be covered by molecules, which indicates the low possibility of multiple molecules binding in the same nanogap at the same time.

Figure 1C,D show representative I–V_g and I–V_b curves measured from the three-terminal junction at different values of V_b and V_g, respectively. The distinct current bi-plateau feature and the linear variation of the switch points and widths of the plateaus with V_g and V_b indicate that the molecular junction has been formed and the current through it can be effectively controlled by V_g and V_b.

3. Results and Discussion

3.1. Current Map Measurements and Calculations

The color-map of the measured current through the SELC as a function of V_b and V_g is shown in **Figure 2**B. The color code divides the map into different transmission regimes. The red and blue colors respectively indicate the positive and negative currents in the resonance regime, where the energy levels of the conductive MOs (ε_1: HOMO-1 and ε_2: HOMO-2, see Section S3 (2), Supporting Information) lie within the bias window, are well-separated, and are conductive due to their coupling to both electrodes (in contrast to ε_0: HOMO, where the long-alkyl chain isolates the Fc-centered level from one electrode). In the map, ε_1 and ε_2 indicate their resonance regions. One distinct characteristic, which is shared by all five different kinds of Fc-based gated SETs (see Section S8, Supporting Information), is evident in Figure 2, showing that ε_1 and ε_2 overlap at around ±100 meV. The left (γ) and right (γ') dashed lines indicate the edges of the ε_1 resonance region. Clear transitions between the resonance regime and the Coulomb blockade regime (white diamond-shaped areas) are shown in the corresponding differential conductance (dI/dV) map of Figure 2D. "1", "3", and "5" indicate the Coulomb blockade regions under different gate voltages near zero-bias. They correspond directly to the energy diagram in Figure 2A, with both MO levels above/below the Fermi energy for region "1"/"5", respectively, and with the electrostatic potential of the leads sandwiched between the two MO levels for region "3", that is, the bias window sits within the energy gap between the two MOs. This creates the diamond-shaped Coulomb blockade region trapped within a ≈100 mV bias voltage range which corresponds to the energy difference between the two MOs (ΔMOs = $\varepsilon_1 - \varepsilon_2$), as marked by the crossing of the ε_1 and ε_2 resonance boundaries. The computed electron transmission spectrum (Ts) overlaid in Figure 2A (state "5") is the zero-bias Ts of the molecular junction calculated by DFT-NEGF method (see Section S3 (2), Supporting Information, for details). The energy difference between the two Ts peaks describes the calculated ΔMOs, which is about 110 meV in good agreement with the measurements and is robust even for different conformations of the molecule and different electrode distances in the SET (see Figures S5 and S6, Supporting Information). The narrow widths of the peaks represent the small broadenings

of the MOs, ensuring small currents in the Coulomb blockade region. Due to the asymmetry of the $-(CH_2)_9-$ and $-(CH_2)_3-$ linkers, the molecule–electrode couplings under positive and negative biases are different, resulting in different extensions of the Ts peaks. Consequently, the background (blockade) current under negative bias voltage is higher than at positive bias (as seen in Figure 2B,C, corresponding to the measured and calculated current maps, respectively). In addition, no Kondo effect was observed in the experiment and the molecule is in the ground state ($S = 0$) (see Section S12, Supporting Information). DFT calculations show the spin degeneracy of the ground state molecule in the absence of magnetic field. The experiments reported in this work were conducted at 225 mK. In our previous work,[25] where similar molecules were studied, well-defined conductance excitations within the Coulomb blockade regime can persist up to 120 K, suggesting that the operations reported in the present work can be feasible at much higher temperatures.

Due to the monotonic evolution of the energy eigenvalues of MOs under bias and gate voltages,[17,39,46] we developed a theoretical model to describe the energy change rates (K_B and K_G) of MOs, which are directly related to the molecular dipole moments along the directions of voltages (see Section S3 (1), Supporting Information, for details). Thus, K_B and K_G can be calculated by the shift rates of Ts under bias and gate voltages, respectively (see Section S3 (3), Supporting Information).[38,39] However, K_B, K_G and the MO energy shift (MOs Shift) are directly related to the configuration and background electrostatic potential of the molecular junction. Thus, to understand the junction configuration in the experiment, we calculated 12 different configurations for the 3-terminal molecular junction of the same molecule (see Section S3 (4), Supporting Information) and analyzed their corresponding K_B, K_G, ΔMOs, and MOs Shift values (see Section S3 (5) Table S1, Supporting Information). The data show that ΔMOs remain near-constant (≈110 meV) for the different configurations, in line with the experimental observations and proving that the Coulomb region lies stably within a well-defined and easily accessed bias voltage range (see Section S4, Supporting Information) despite the potentially shifted current maps for different junction configurations. Indeed, the experimental K_B and K_G can be extracted from the slopes of γ and γ' edges for both MO resonance regions[17] as (see Section S3 (5), Supporting Information, for details): $K_B = (\gamma + \gamma')/2(\gamma - \gamma')$, $K_G = -\gamma\gamma'/(\gamma - \gamma')$. Figure 2F,G illustrate the combined modulation of the shifts of ε_1 energy level in terms of the energy change rates K_B and K_G.

The corresponding DFT-NEGF calculated current and differential conductance (dI/dV) maps of the junction (see Section S3 (6), Supporting Information, for details) are shown in Figure 2C,E, respectively. The Ts not only reproduces the asymmetric background of Coulomb blockade regions under bias reversal, but also resolves the different widths of the γ and γ' edges (see Figure 2E,D), which can be understood by the directional shift of the Ts towards the bias window controlled by the gate voltage (note the asymmetric Ts peaks in Figure 2A "5", discussed in Section S3 (6), Supporting Information). Since the K_B and K_G values correspond directly to the electronic structure of the conductive MOs, they reflect the dipole moments of each MO. The similarity between the experiment and theoretical
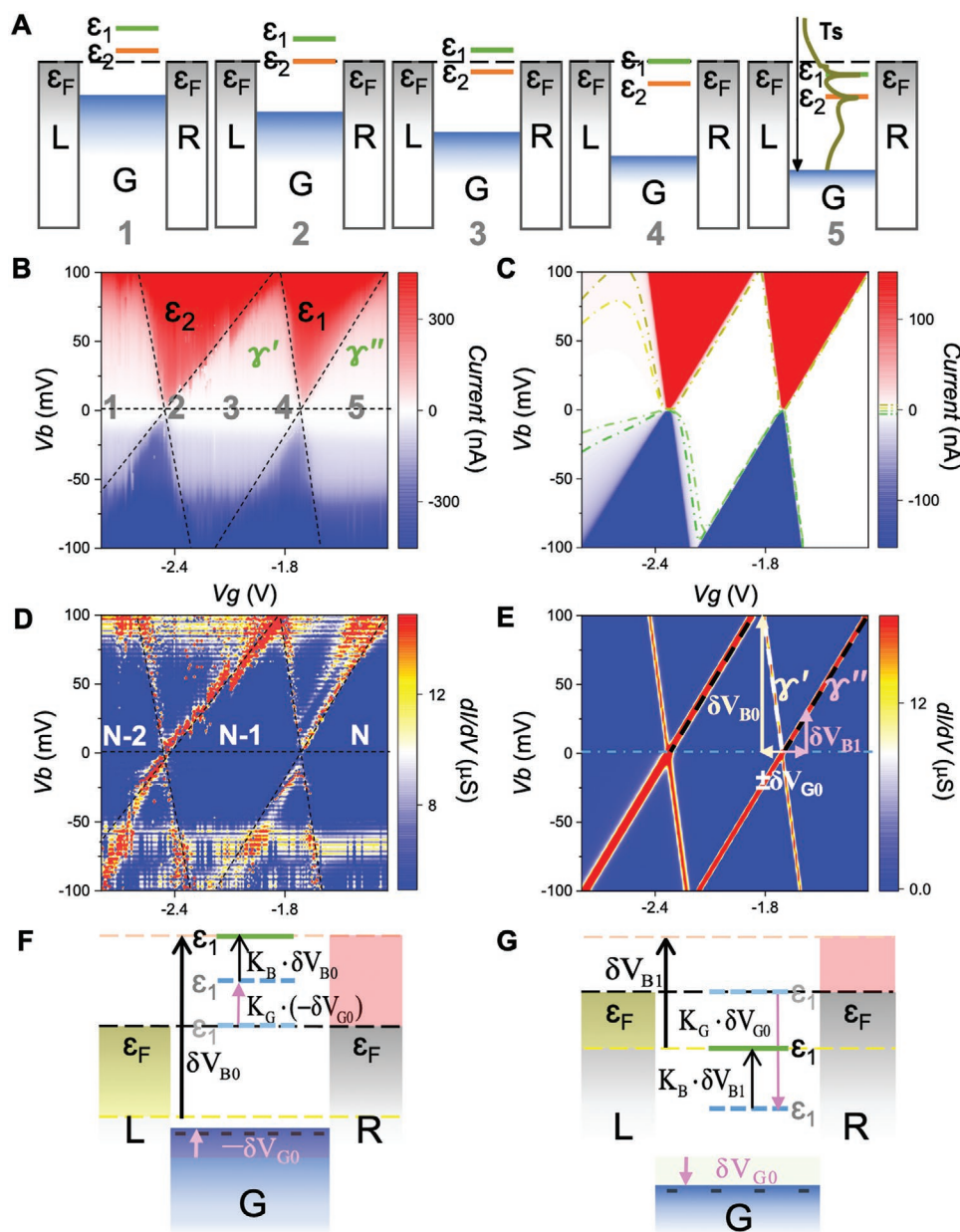
ADVANCED
SCIENCE NEWS
www.advancedsciencenews.com

ADVANCED
MATERIALS
www.advmat.de

Figure 2. The current modulation of SELC. A) Schematic diagrams of the shift of MOs manipulated by the gate voltage at zero-bias. The Ts of state "5" indicates that the conductive MOs (ε_1: HOMO-1, ε_2: HOMO-2) is below the Fermi energy when V_g is close to zero. At charge points "2" and "4", ε_1 and ε_2 are respectively aligned with the Fermi level of the electrodes. B) Measured current map at 225 mK with V_b: 231 × V_g: 231 points. The red/blue colors indicate positive/negative resonance currents, respectively. The numbers correspond to the diagrams in (A). ε_1 and ε_2 resonance regions correspond to the MOs. C) Calculated current map with V_b: 101 × V_g: 142 points (V_b: 2 mV per step; V_g: 11 mV per step). The background pattern (marked by the dashed contour lines) is contributed by the extension of transmission peaks. D) Measured differential conductance map highlighting the edges between resonance and Coulomb blockade regimes. "N-2", "N-1" and "N" indicate the number of fully occupied MOs. E) The calculated differential conductance map. $-\delta V_{G0}$ and $+\delta V_{G0}$ indicate charging and discharging of the Gate. δV_{B0} and δV_{B1} indicate the increase of V_b from 0 V to γ' and γ'' edges, respectively. F,G) Schematics showing how the energy of ε_1 MO modulated by V_b and V_g aligns with the right and left electrode Fermi levels. The light blue dashed line indicates the initial energy of ε_1. The dark blue dashed line indicates the energy of ε_1 when V_g changes $-\delta V_{G0}$ (F) or $+\delta V_{G0}$ (G). The green line indicates the final energy of ε_1 after adding the change of V_b (δV_{B0} or δV_{B1}). K_B and K_G are the energy change rates.

calculations on the parallel evolution of the two MOs along the gate-bias voltage (see Figure S6, Supporting Information) is a good indication of the presence of a single molecule in the junction. Two independent molecules, for example, would present very different slopes due to substantial differences of the

coupling to the electrodes at the microscopic level.[31] Thus, the agreement between the theoretical calculations and experimental measurements (data for different Fc-based SETs are shown in Section S8, Supporting Information) strongly demonstrates that the electrostatic modulation of the two conductive

MOs of the Fc moiety provides a two-state Coulomb blockade region at $V_b = 1$–100 mV. The differences between the theoretical current map (Figure 2C) and the measured results (Figure 2B) are due to the effect of the gate voltage field on the molecular configuration, the leaking currents from the source/drain to the gate electrode, and the inelastic electron tunneling (IET) current of the molecule, which are all effects not considered in the calculations. As discussed in Section S7, Supporting Information, Figure 2B shows the current shift in the high gate voltage region ($|V_g| > 2.2$ V), which is caused by a small change in the molecular configuration under high gate electrostatic field. Furthermore, the current in the Coulomb blockade region of Figure 2B is >0.1 nA resulting from leakage through the gate (see Section S11, Supporting Information), while the blockade current in the theoretical case can be <10^{-3} nA. Finally, the measured IET spectra and corresponding vibrational modes shown in Section S9, Supporting Information, also provide strong evidence that an individual molecule is responsible for the transport behavior.

3.2. Working Principle of the Resettable SELC

Using the two-state diamond-shaped Coulomb blockade feature provided by the two MOs, we establish SELC by using the current as Output signal, and the gate (Input1: V_g) and the bias (Input2: V_b) voltages as two orthogonal Input signals. **Figure 3** summarizes the working principle of our SELC. Figure 3A shows the detailed current map. Four input ranges of V_g and three of V_b are determined based on the current oscillation signal (see Section S5, Supporting Information) across the Coulomb diamond region, labeled A (-1.82 V "0" to -2.02 V "1"), A' (-1.67 V "0" to -1.82 V "1"), A" (-1.77 V "0" to -1.82 V "1"), AA' (-1.67 V "0" to -2.02 V "1") and B (70 mV "0" to 80 mV "1"), B' (30 mV "0" to 70 mV "1"), BB' (30 mV "0" to 80 mV "1"). The (1,1) input represents the V_g and V_b both at high states in their own ranges, which is opposite to the (0,0) input, for instance. Correspondingly the (1,0) input means that the V_g is at high state while the V_b is at low state, opposite to the (0,1) input. The current (Output) is represented by the color code in the map, red indicating high current state (>300 nA, "on", "1") and blue the low current state (<300 nA, "off", "0"). The white rectangles indicate logic operation areas, defined by two orthogonal input ranges (i.e., one V_g range and one V_b range). The horizontal/vertical black dashed arrows represent the operating ranges of the gate/bias voltage under a particular bias/gate voltage.

We take the 2-input logic operation along AA' and BB' as an example to introduce the working principle of the logic gates
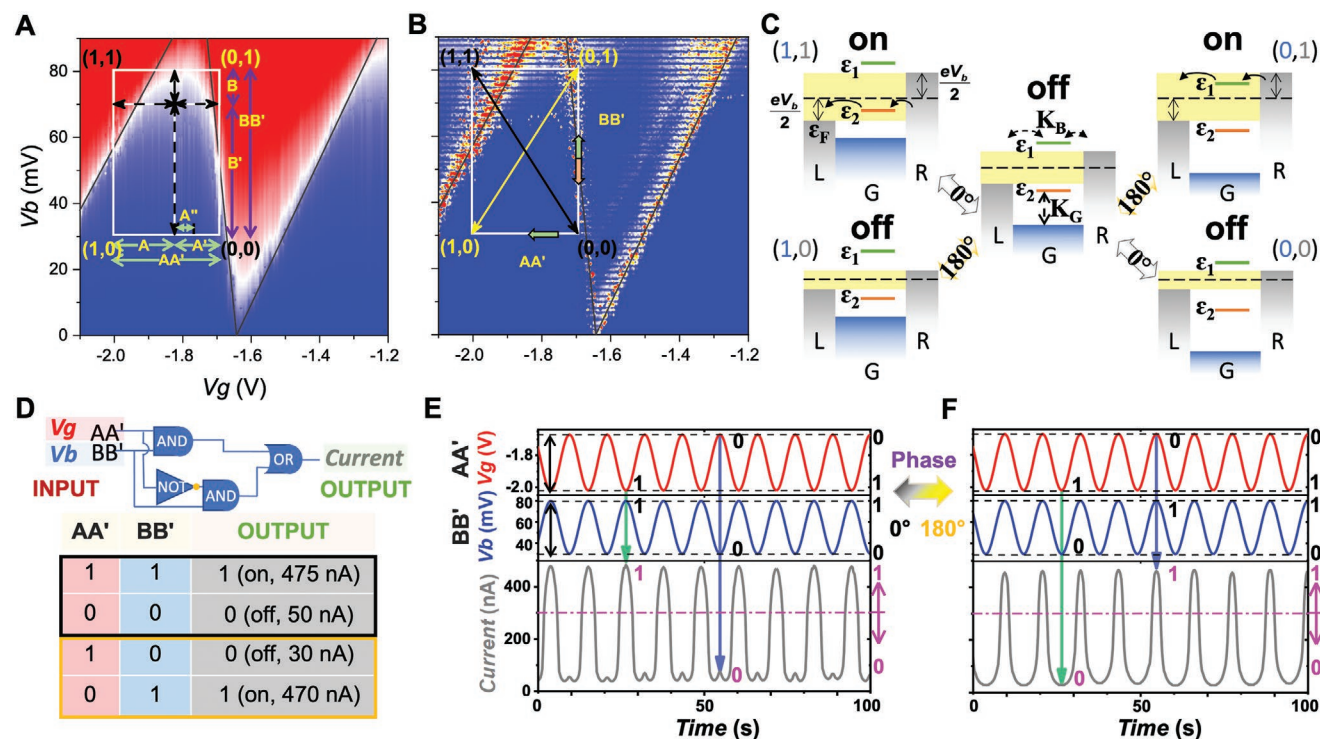

Figure 3. Logic calculation based on resonance excitations of MOs. A) Measured 231 × 231 points current map at 225 mK marked with logic operating voltage-ranges. A, A', A", AA' and B, B', BB' are the voltage-ranges of input-gate and input-bias, respectively. The white rectangles mark 2-input logic operation areas. Input (1,1) means high-gate and high-bias voltages, (0,0) is the opposite case. Input (1,0) means high-gate and low-bias voltages, (0,1) is the opposite. B) Differential conductance map corresponding to (A). Input AA'-BB' is an example to illustrate how gate (V_g) and bias (V_b) voltages are combined to achieve logic operations. The black arrow goes from (0,0) to (1,1), when V_g and V_b both change along the short green arrows. The yellow arrow goes from (0,1) to (1,0), when V_b and V_g change along the short orange and green arrows, respectively. C) The schematic diagrams describe the energy level distributions of the four input cases in (B). Phase 0° and 180° correspond to the black and yellow arrow, respectively. D) Equivalent logic circuit and truth table with AA'-BB' inputs at 0° and 180° phases. E,F) show the curves of input V_g and V_b and measured output current at 0° and 180°, respectively.

ADVANCED
SCIENCE NEWS
www.advancedsciencenews.com

ADVANCED
MATERIALS
www.advmat.de

within a set operating area. Figure 3B is the corresponding logic diagram in the differential conductance map. The arrows in the white rectangle illustrate how V_g and V_b are combined to govern the current switching across the edges of the resonance and Coulomb blockade regions. The black arrow indicates that the changes of V_g (along the short-green-left arrow of AA′) and V_b (along the short-green-up arrow of BB′) are in the same phase (0°). The corresponding multi-cycle logic input and output signals are shown in Figure 3E. As the input gate signal and input bias signal change in phase from (0,0) to (1,1), the signal of output current changes from "0" (off) to "1" (on). Thus, high V_g and high V_b inputs (1,1) lead to high output current "1", while low V_g and low V_b inputs (0,0) lead to low output current "0". However, when the change of V_g (along the short-green-left arrow of AA′) and V_b (along the short-orange-down arrow of BB′) are out of phase (180°), the logic operation changes (Figure 3F). In this case, as V_g and V_b change from (0,1) to (1,0), output current changes from "1" (on) to "0" (off).

Figure 3C schematically shows the energy distributions of MOs (ε_1 and ε_2) under the voltages indicated by black and yellow arrows in Figure 3B. The two orthogonal inputs switch the output current by shuttling the MOs in and out of the bias window. The central diagram corresponds to the intersection of the arrows. The four diagrams on the corners correspond to the four terminals of the arrows (1,1), (0,0), (1,0), and (0,1). The top two diagrams show the resonance states, where ε_1 or ε_2 is in the bias window, generating high-current "on" states (>300 nA, output = "1"). The rest belong to the Coulomb blockade regime,

with no MO in the bias window. They correspond to low-current "off" states (<300 nA, output = "0"). This logic operation is illustrated in the truth table in Figure 3D and repeated for several cycles in Figure 3E,F to show the stability of SELC. Note that the signal remained stable throughout the whole experiment for about 2 months, even independent of the scan rate variation of the input signal, see Figure S12, Supporting Information. At least 37 cycles were taken for each curve, see Figure S11, Supporting Information; for illustrative purposes only 9 cycles (40 points per cycle) are shown in Figure 3. The result of this logic operation can be interpreted as a complex logic gate array of one "INH" gate (inhibit) and one "AND" gate feeding their outputs into an "OR" gate. In this logic operation, SELC acts as a high-bias voltage indicator, that is, a high-bias input produces a high-current output, while a low-bias input produces a low-current output. The on/off ratio of high and low output currents is ≈10.

3.3. SELC 1-Input Logic Gates

For the 1-input logic gates, V_g is the only input, current is the output, and V_b is fixed at 70 mV. **Figure 4**A shows V_g ranges A and A′ for 1-input logic gates "YES" and "NOT", respectively. Figure 4B,C shows corresponding electronic symbols, truth tables, and Input/Output signals. The 1-input "YES" logic gate is based on current switching between the ε_2 resonance regime and the Coulomb blockade region. In this case, the high V_g ("1",
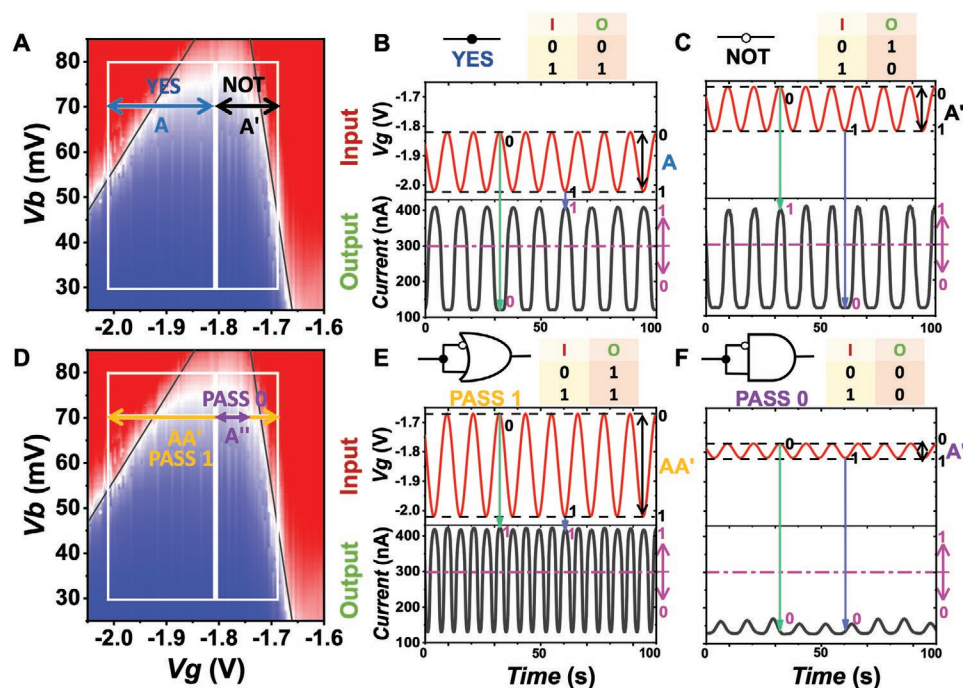

Figure 4. Four resettable universal 1-input logic gates. In (A,D), input gate voltages with A, A′, AA′ and A″ ranges are marked on the current maps, which indicate 1-input "YES", "NOT", "PASS 1", and "PASS 0" logic gates. B) Equivalent circuit, truth table, and corresponding Input/Output signal for 1-input "YES" gate. With the gate voltage change from −2.02 V "1" to −1.82 V "0", the current changes from 410 nA "1" to 120 nA "0". C) For 1-input "NOT" gate, with gate voltage change from −1.82 V "1" to −1.67 V "0", the current changes from 120 nA "0" to 405 nA "1". E) For 1-input "PASS 1" gate, with the gate voltage change from −2.02 V "1" to −1.67 V "0", the current changes from 410 nA "1" to 405 nA "1". The frequency of the current signal is doubled compared with the input gate signal. F) For 1-input "PASS 0" gate, with the gate voltage change from −1.82 V "1" to −1.77 V "0", the current changes from 120 nA "0" to 130 nA "0". All 1-Input logic gates operate at 70 mV bias.

**ADVANCED
SCIENCE NEWS**

www.advancedsciencenews.com

**ADVANCED
MATERIALS**

www.advmat.de

–2.02 V) leads to resonance conductance of ε_2 MO, resulting in high current ("1", ≈410 nA). The low V_g ("0", –1.82 V) reduces the energy of ε_2 MO and moves it out of the bias window, resulting in current blockade ("0", ≈120 nA). Thus, high-input leads to high-output and low-input leads to low-output, "YES" logic. Conversely, for the 1-input "NOT" logic gate the operation is based on current switching between the Coulomb blockade region and the ε_1 resonance regime. In this case, at the high V_g ("1", –1.82 V) no MO lies in the bias window, so the current is in the blockade region ("0", ≈120 nA). The low V_g ("0", –1.67 V) further reduces the energy of MOs and shifts ε_1 into the bias window, so the current is in the resonance region ("1", ≈410 nA). Thereby, high-input leads to low-output and low-input leads to high-output, "NOT" logic.

Figure 4D shows the V_g ranges AA′ and A″ for 1-input logic gates "PASS 1" and "PASS 0", respectively. According to the discussion above, the 1-input "PASS 1" logic gate involves current switching between ε_2 and ε_1 resonance regimes. Both high and low inputs led to high outputs, "PASS 1" logic. Since the switching process of the output current spans the entire Coulomb blockade region, the frequency of the output current signal is doubled compared with the input gate signal. This interesting feature can be used as a frequency multiplier. The current signal is also used as an address for the logic operations to define the Coulomb diamond region, which provides important information for calibrating the V_g ranges (see Section S5, Supporting Information, for details). By contrast, the 1-input "PASS 0" logic gate is based on the stability of the blockade current. In this case, at both high ("1", –1.82 V) and low ("0", –1.77 V) V_g, the two MOs are distributed on both sides of the bias window (as shown in Figure 3C-"off"), so the output current is in the Coulomb blockade region ("0", ≈120 nA) contributed by the extension between the two transmission peaks of Ts (shown as Figure 2A "5"). High-input and low-input both lead to low-outputs, "PASS 0" logic.

3.4. SELC 2-Input Logic Gates

Based on the gate voltage ranges of the 1-input logic gates, bias voltage control is added, so that all seven universal 2-input logic gates can be realized, as demonstrated in **Figure 5**. In the 2-input logic gates, gate voltage is Input-signal 1, and bias voltage is Input-signal 2. The main difference between the operation of 2-input and 1-input logic gates is the phase control. The 2-input logic gate contains two input signals, and the phase difference between them determines the moving direction of the MOs relative to the bias window, thereby affecting the state of the output current. Thus, phase control combined with different operating voltage makes it possible to realize all 2-input universal logic gates.

Figure 5A shows the 2-input "AND" gate. Its operation area is defined by A-B′ in both 0° and 180° phases. The input ranges of V_g and V_b are shown on the current map. The graphs on the right are the Input/Output signals in 0° and 180° phases, respectively. In 0° phase, by changing V_g (Input-1, red curve) from –2.02 V "1" to –1.82 V "0" (range A) and changing V_b (Input-2, blue curve) from 70 mV "1" to 30 mV "0" (range B′), the current (Output, gray curve) changes from 400 nA "1" to

25 nA "0", that is, (1,1) → 1, (0,0) → 0. In 180° phase, as V_g changes from "1" to "0" (A) and V_b changes from "0" to "1" (B′), the current changes from 40 nA "0" to 120 nA "0", that is, (1,0) → 0, (0,1) → 0. "AND" gate works as a Carry in a Half-adder logical circuit that performs an addition operation on two binary digits.

Figure 5B shows the "INH" gate. Its operation area is defined by A′-B′ in both 0° and 180° phases. In 0° phase by changing V_g from –1.82 V "1" to –1.67 V "0" (range A′) and changing V_b from 70 mV "1" to 30 mV "0" (range B′), the current changes from 120 nA "0" to 50 nA "0", that is, (1,1) → 0, (0,0) → 0. In 180° phase, by changing V_g from "1" to "0" (A′) and changing V_b from "0" to "1" (B′), the current changes from 25 nA "0" to 420 nA "1", that is, (1,0) → 0, (0,1) → 1. It works as a Borrow in Half-subtractor.

Figure 5C,D show the "XOR" and "XNOR" gates, respectively. They have different input voltage ranges in different phases. For the "XOR" gate in 0° phase, as V_g changes from –1.82 V "1" to –1.67 V "0" (A′) and V_b changes from 80 mV "1" to 30 mV "0" (BB′), current changes from 230 nA "0" to 75 nA "0", that is, (1,1) → 0, (0,0) → 0. At 180° phase, as V_g changes from –2.02 V "1" to –1.67 V "0" (AA′) and V_b changes from 70 mV "0" to 80 mV "1" (B), current changes from 400 nA "1" to 480 nA "1", that is, (1,0) → 1, (0,1) → 1. Notably, the input gate voltage and bias voltage in both phases have the same minimum value of –1.67 V and the same maximum value of 80 mV, respectively. This means that only the amplitudes of the input voltage ranges are changed with the phase. It works as a Sum in Half-adder and Diff. in Half-subtractor. For the "XNOR" gate, with AA′ and B inputs in 0° phase, current changes from 480 nA "1" to 420 nA "1", that is, (1,1) → 1, (0,0) → 1. In 180° phase, the corresponding inputs are A and BB′, and current changes from 25 nA "0" to 200 nA "0", that is, (1,0) → 0, (0,1) → 0. The input gate voltage and bias voltage in both phases have the same maximum value of –2.02 V and 80 mV, respectively.

Figure 5E–G show the "NAND", "NOR", and "OR" gates. These three logic gates have the same bias voltage range in both phases, only the gate voltage range changes with phase. To avoid repetition, we omitted the curves of the input signals and kept only the input voltage range and Boolean states. For "NAND" gate, the inputs in 0° phase are A′ for V_g and B for V_b. The current changes from 200 nA "0" to 420 nA "1", that is, (1,1) → 0, (0,0) → 1. The inputs in 180° phase are AA′ and B. The current changes from 400 nA "1" to 480 nA "1", that is, (1,0) → 1, (0,1) → 1. For "NOR" gate, the Input/Output signal in 0° phase are the same with "NAND" gate (A′-B), that is, (1,1) → 0, (0,0) → 1. The inputs in 180° phase are A″ and B. The current changes from 120 nA "0" to 210 nA "0", that is, (1,0) → 0, (0,1) → 0. For "OR" gate, the inputs in 0° phase are A for V_g and B for V_b. The current changes from 480 nA "1" to 120 nA "0", that is, (1,1) → 1, (0,0) → 0. In 180° phase, the input ranges are AA′ and B, the same as "NAND" and "XOR" gates, that is, (1,0) → 1, (0,1) → 1. To clearly show the relationship between the input and output signals, two cycles are shown in Figure 5. The multi-cycle output curves for the 2-input logic gates are shown in Figure S10, Supporting Information.

From Figure 5 it is clear that SELC can realize all the universal 2-input logic gates within one gated single-molecule junction, in contrast to conventional CMOS (see Section S10,
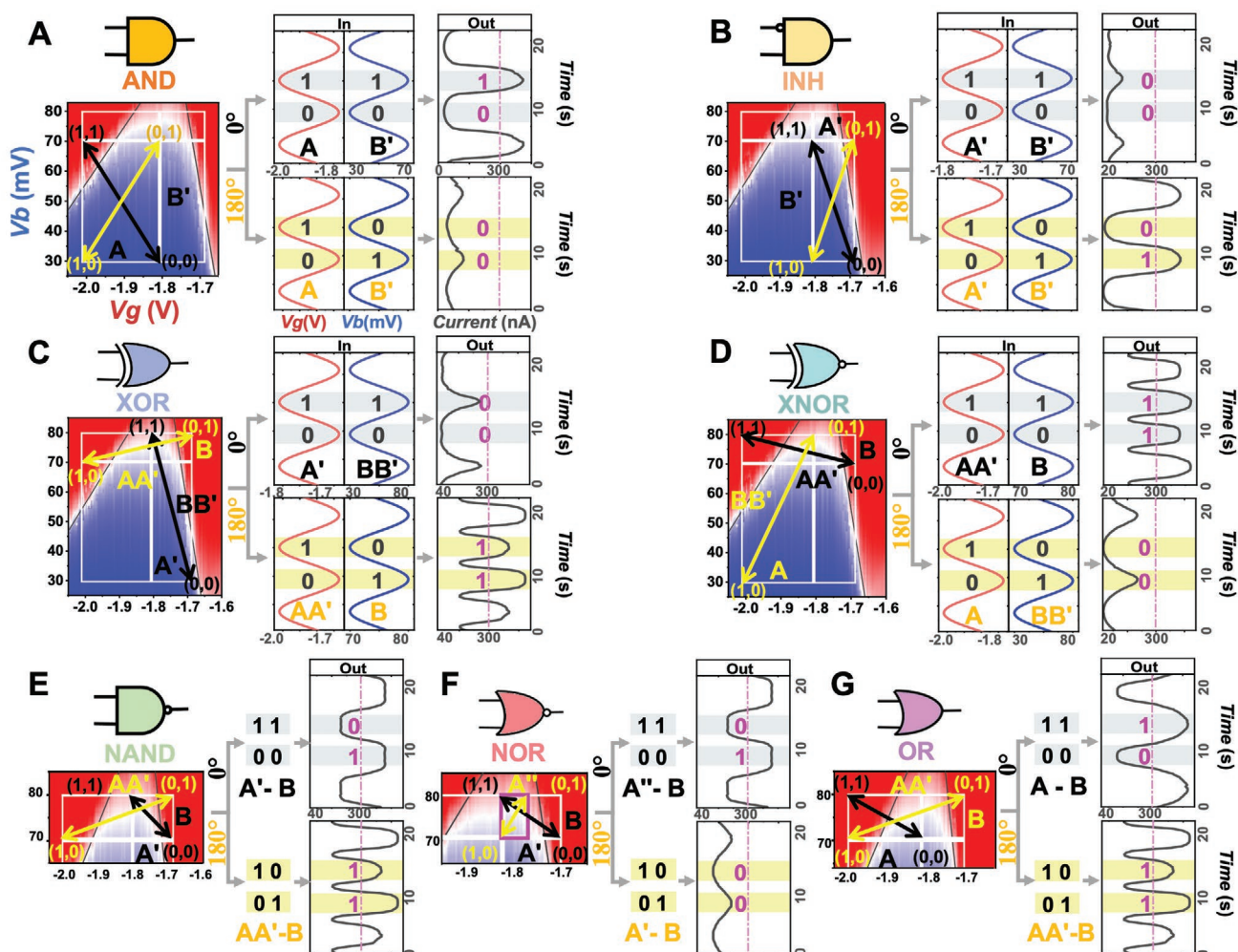
ADVANCED
SCIENCE NEWS
www.advancedsciencenews.com

ADVANCED
MATERIALS
www.advmat.de

Figure 5. Seven resettable universal 2-Input logic gates. A,B) "AND" and "INH" logic gates with A-B′ and A′-B′ inputs in both phases, respectively. The black and yellow arrows in current map are corresponding to the Input/Output signals in 0° phase and 180° phase, respectively. C) "XOR" logic gate with A′-BB′ input in 0° phase and AA′-B input in 180° phase. The input gate voltages in both phases have the same minimum value and the input bias voltages in both phases have the same maximum value, that is, the (0,1) point is the same in the voltage ranges in both phases. The highest gate voltage and the lowest bias voltage (i.e., the (1,0) point) from 0° phase to 180° phase are changed. D) "XNOR" logic gate with AA′-B input in 0° phase and A-BB′ input in 180° phase. The input gate and bias voltages in both phases have the same maximum value, that is, the (1,1) point is the same in the voltage ranges in both phases. The lowest gate voltage and the lowest bias voltage (i.e., the (0,0) point) from 180° phase to 0° phase are changed. E–G) "NAND", "NOR", and "OR" logic gates have the same input bias voltage range in both phases and change the gate voltage range with phase only. "NAND" has A′-B input in 0° phase and AA′-B input in 180° phase. "NOR" has A′-B input in 0° phase and A″-B input in 180° phase. "OR" has A-B input in 0° phase and AA′-B input in 180° phase.

Supporting Information). It allows dynamic logic circuits to be scaled down to a few nanometers, and the single-junction design greatly reduces charge leakage, charge sharing, and back-gate coupling between devices. Crucially, only a 2 V gate voltage (CMOS is in the 3~15 V range) and 100 mV drive voltage (well below the 1.5~5 V of CMOS) are required to run the SELC.

4. Conclusion

We report molecular-scale SELC in a three-terminal SET by utilizing adjacent conductive MOs provided by a single Fc-based molecule. Its operating principle is based on predictable and

reliable current conversions modulated by voltages crossing the stable Coulomb blockade regime, avoiding dependence on absolute current and improving function reproducibility. Compared with other approaches,[24,26,27,32,33,57] the non-conjugated asymmetric Fc-based molecule naturally provides logic operations via its robust and unique Coulomb blockade characteristics. The isolation provided by the asymmetric *n*-alkyl ($n \geq 3$) linkers on either side of the Fc moiety ensures narrow MO levels, efficiently suppressing current in the Blockade regime and enabling encoding of information via orthogonal modulation for the realization of sophisticated operation functions. This results in clear and multi-cycle stable current signals controlled by two orthogonal electrostatic fields, enabling in situ implementation of all four universal 1-input and all seven

universal 2-input logic gates in a single molecule with high stability. Through phase control of an external circuit, the benefits of implementing multiple logic operations within a single molecule (instead of connecting several separate devices with switching characteristics in series) are low charge leakage, with no mutual interference, small functional area (≈2 nm), low operating voltage (because the applied potential only drops over one element[5]) and simple device construction. Crucially, our design can be extended to multi-channel mesoscopic Coulomb blockade systems, field-effect single molecules, or molecular layers, with promising future applications of SELC in realizing multifunctional nanodevices including frequency multipliers, diodes, switches, voltage indicators, and calculators, among others.

5. Experimental Section

Synthesis of the Molecule: Previously reported procedures were followed[16,25,58] to synthesize and characterize AcS-$(CH_2)_3$-Fc-$(CH_2)_9$-SAc and AcS-$(CH_2)_6$-Fc-$(CH_2)_6$-SAc as described in Section S1, Supporting Information.

Sample Preparation for SELCs: The previously reported method[25] was followed to fabricate the chip with nanowires and back-gates, as presented in Section S2, Supporting Information. After the chip has been properly fabricated, it was immersed into the diluted molecular solution (dissolved in ethanol) for about 30–40 min to allow the molecules to adsorb to the surface of the gold nanowire. The chip was then gently washed several times with the molecular solution, then washed with ethanol and blow-dried with N_2 to remove excess molecular solution to ensure that the remaining molecules were firmly attached to the gold surface. The chip on the chip holder was mounted in a home-made probing box, which can be used for current feedback-controlled electromigration, to narrow the nanowire into single-atom-contact nanoelectrodes (see Section S2 and Figure S3, Supporting Information). The whole process was carried out in a nitrogen-filled environment at room temperature and standard atmospheric pressure. After the nanoelectrodes formed, the chip was transferred to a Helium-3 cryostat for measurements at low temperature. The base temperature of the cryostat (225 mK) was used for convenience, as these measurements could be done at LN_2 temperatures.

The Current Measurements: The current through the SELC as a function of bias and gate voltages was measured via a Keithley 6430 Source Meter by applying the bias voltage on the Au electrodes in DC. The gate voltage was applied through the Al_2O_3/Al gate and controlled by a Keithley 2400. The SELCs were mounted on the chip holder in a vacuum tube and placed in vacuum inside the sample holder of the Helium-3 cryostat.

DFT-NEGF Calculations: The transmission spectra (Ts) of different structures of the Al_2O_3/Al gated Au/S$(CH_2)_3$Fc$(CH_2)_9$S/Au junction were calculated using the DFT-NEGF method implemented in the Atomistix ToolKit (ATK)[59] package (see Section S3 (2), Supporting Information, for details). Based on these Ts, the theoretical modulation parameters of the MOs of different structures by the bias voltage and the gate voltage were calculated (see Section S3 (3), Supporting Information, for details). The mechanisms of the modulation were defined by the theoretical model (see Section S3 (1), Supporting Information, for details). The comparison between measured parameters and calculated parameters is shown in Table S1, Supporting Information (see Section S3 (5), Supporting Information). The calculated current map was drawn by integrating Ts as a function of bias voltage and gate voltage. The values of K_B, K_G, and MOs Shift in Exp.1 in Table S1, Supporting Information, are used in the integration. The Ts under positive bias and negative bias are represented by Ts calculated at 100 and −100 mV, respectively (see Section S3 (6), Supporting Information).

Supporting Information

Supporting Information is available from the Wiley Online Library or from the author.

Conflict of Interest

The authors declare no conflict of interest.

Data Availability Statement

The data that support the findings of this study are available from the corresponding author upon reasonable request.

[1] X. Chen, M. Roemer, L. Yuan, W. Du, D. Thompson, E. Del Barco, C. A. Nijhuis, *Nat. Nanotechnol.* **2017**, *12*, 797.

[2] C. Guo, K. Wang, E. Zerah-Harush, J. Hamill, B. Wang, Y. Dubi, B. Xu, *Nat. Chem.* **2016**, *8*, 484.

[3] C. Jia, A. Migliore, N. Xin, S. Huang, J. Wang, Q. Yang, S. Wang, H. Chen, D. Wang, B. Feng, Z. Liu, G. Zhang, D.-H. Qu, H. Tian, M. A. Ratner, H. Q. Xu, A. Nitzan, X. Guo, *Science* **2016**, *352*, 1443.

[4] S. Kumar, M. Merelli, W. Danowski, P. Rudolf, B. L. Feringa, R. C. Chiechi, *Adv. Mater.* **2019**, *31*, 1807831.

[5] Y. Han, C. Nickle, Z. Zhang, H. Astier, T. J. Duffin, D. Qi, Z. Wang, E. Del Barco, D. Thompson, C. A. Nijhuis, *Nat. Mater.* **2020**, *19*, 843.

[6] L. Bogani, W. Wernsdorfer, *Nat. Mater.* **2008**, *7*, 179.

[7] S. Cai, W. Deng, F. Huang, L. Chen, C. Tang, W. He, S. Long, R. Li, Z. Tan, J. Liu, J. Shi, Z. Liu, Z. Xiao, D. Zhang, W. Hong, *Angew. Chem., Int. Ed.* **2019**, *58*, 3829.

[8] W. H. Soe, C. Manzano, A. De Sarkar, F. Ample, N. Chandrasekhar, N. Renaud, P. de Mendoza, A. M. Echavarren, M. Hliwa, C. Joachim, *Phys. Rev. B* **2011**, *83*, 155443.

[9] C. Joachim, N. Renaud, M. Hliwa, *Adv. Mater.* **2012**, *24*, 312.

[10] N. Zhang, W. Y. Lo, A. Jose, Z. Cai, L. Li, L. Yu, *Adv. Mater.* **2017**, *29*, 1701248.

[11] F. Meng, Y. M. Hervault, Q. Shao, B. Hu, L. Norel, S. Rigaut, X. Chen, *Nat. Commun.* **2014**, *5*, 3023.

[12] Y. Liu, A. Offenhausser, D. Mayer, *Angew. Chem., Int. Ed.* **2010**, *49*, 2595.

[13] P. Gehring, J. M. Thijssen, H. S. J. van der Zant, *Nat. Rev. Phys.* **2019**, *1*, 381.

[14] S. Goswami, S. P. Rath, D. Thompson, S. Hedstrom, M. Annamalai, R. Pramanick, B. R. Ilic, S. Sarkar, S. Hooda, C. A. Nijhuis, J. Martin, R. S. Williams, S. Goswami, T. Venkatesan, *Nat. Nanotechnol.* **2020**, *15*, 380.

[15] W. Du, T. Wang, H.-S. Chu, C. A. Nijhuis, *Nat. Photonics* **2017**, *11*, 623.

[16] L. Yuan, N. Nerngchamnong, L. Cao, H. Hamoudi, E. del Barco, M. Roemer, R. K. Sriramula, D. Thompson, C. A. Nijhuis, *Nat. Commun.* **2015**, *6*, 6324.

[17] H. Song, Y. Kim, Y. H. Jang, H. Jeong, M. A. Reed, T. Lee, *Nature* **2009**, *462*, 1039.

[18] S. Zhang, C. Guo, L. Ni, K. M. Hans, W. Zhang, S. Peng, Z. Zhao, D. C. Guhr, Z. Qi, H. Liu, M. Song, Q. Wang, J. Boneberg, X. Guo, T. Lee, E. Scheer, D. Xiang, *Nano Today* **2021**, *39*, 101226.

[19] H. Park, J. Park, A. K. L. Lim, E. H. Anderson, A. P. Alivisatos, P. L. McEuen, *Nature* **2000**, *407*, 57.

[20] J. Park, A. N. Pasupathy, J. I. Goldsmith, C. Chang, Y. Yaish, J. R. Petta, M. Rinkoski, J. P. Sethna, H. D. Abruna, P. L. McEuen, D. C. Ralph, *Nature* **2002**, *417*, 722.

[21] W. Liang, M. P. Shores, M. Bockrath, J. R. Long, H. Park, *Nature* **2002**, *417*, 725.

[22] S. J. van der Molen, J. Liao, T. Kudernac, J. S. Agustsson, L. Bernard, M. Calame, B. J. van Wees, B. L. Feringa, C. Schonenberger, *Nano Lett.* **2009**, *9*, 76.

[23] J. Zhou, K. Wang, B. Xu, Y. Dubi, *J. Am. Chem. Soc.* **2018**, *140*, 70.

[24] L. Yuan, L. Wang, A. R. Garrigues, L. Jiang, H. V. Annadata, M. A. Antonana, E. Barco, C. A. Nijhuis, *Nat. Nanotechnol.* **2018**, *13*, 322.

[25] A. R. Garrigues, L. Wang, E. Del Barco, C. A. Nijhuis, *Nat. Commun.* **2016**, *7*, 11595.

[26] P. Gehring, J. K. Sowa, C. Hsu, J. de Bruijckere, M. van der Star, J. J. Le Roy, L. Bogani, E. M. Gauger, H. S. J. van der Zant, *Nat. Nanotechnol.* **2021**, *16*, 426.

[27] S. Kubatkin, A. Danilov, M. Hjort, J. Cornil, J. L. Brédas, N. Stuhr-Hansen, P. Hedegård, T. Bjørnholm, *Nature* **2003**, *425*, 698.

[28] P. Gehring, J. K. Sowa, J. Cremers, Q. Wu, H. Sadeghi, Y. Sheng, J. H. Warner, C. J. Lambert, G. A. D. Briggs, J. A. Mol, *ACS Nano* **2017**, *11*, 5325.

[29] P. Puczkarski, P. Gehring, C. S. Lau, J. Liu, A. Ardavan, J. H. Warner, G. A. D. Briggs, J. A. Mol, *Appl. Phys. Lett.* **2015**, *107*, 133105.

[30] P. Gehring, M. van der Star, C. Evangeli, J. J. Le Roy, L. Bogani, O. V. Kolosov, H. S. J. van der Zant, *Appl. Phys. Lett.* **2019**, *115*, 073103.

[31] H. B. Heersche, Z. de Groot, J. A. Folk, H. S. van der Zant, C. Romeike, M. R. Wegewijs, L. Zobbi, D. Barreca, E. Tondello, A. Cornia, *Phys. Rev. Lett.* **2006**, *96*, 206801.

[32] S. Caneva, M. Hermans, M. Lee, A. Garcia-Fuente, K. Watanabe, T. Taniguchi, C. Dekker, J. Ferrer, H. S. J. van der Zant, P. Gehring, *Nano Lett.* **2020**, *20*, 4924.

[33] P. Gehring, A. Harzheim, J. Spiece, Y. Sheng, G. Rogers, C. Evangeli, A. Mishra, B. J. Robinson, K. Porfyrakis, J. H. Warner, O. V. Kolosov, G. A. D. Briggs, J. A. Mol, *Nano Lett.* **2017**, *17*, 7055.

[34] D. Goldhaber-Gordon, H. Shtrikman, D. Mahalu, D. Abusch-Magder, U. Meirav, M. A. Kastner, *Nature* **1998**, *391*, 156.

[35] J. J. Parks, A. R. Champagne, G. R. Hutchison, S. Flores-Torres, H. D. Abruna, D. C. Ralph, *Phys. Rev. Lett.* **2007**, *99*, 026601.

[36] X. Guo, Q. Zhu, L. Zhou, W. Yu, W. Lu, W. Liang, *Nat. Commun.* **2021**, *12*, 1566.

[37] B. Fu, M. A. Mosquera, G. C. Schatz, M. A. Ratner, L. Y. Hsu, *Nano Lett.* **2018**, *18*, 5015.

[38] S. Alavi, B. Larade, J. Taylor, H. Guo, T. Seideman, *Chem. Phys.* **2002**, *281*, 293.

[39] T. Seideman, H. Guo, *J. Theor. Comput. Chem.* **2003**, *02*, 439.

[40] X. Wang, L. Cong, D. Zhu, Z. Yuan, X. Lin, W. Zhao, Z. Bai, W. Liang, X. Sun, G.-W. Deng, K. Jiang, *Nano Res.* **2020**, *14*, 1156.

[41] S. J. Kim, J. J. Lee, H. J. Kang, J. B. Choi, Y. S. Yu, Y. Takahashi, D. G. Hasko, *Appl. Phys. Lett.* **2012**, *101*, 183101.

[42] S. J. Shin, J. J. Lee, H. J. Kang, J. B. Choi, S. R. Yang, Y. Takahashi, D. G. Hasko, *Nano Lett.* **2011**, *11*, 1591.

[43] M. El Abbassi, M. L. Perrin, G. B. Barin, S. Sangtarash, J. Overbeck, O. Braun, C. J. Lambert, Q. Sun, T. Prechtl, A. Narita, K. Müllen, P. Ruffieux, H. Sadeghi, R. Fasel, M. Calame, *ACS Nano* **2020**, *14*, 5754.

[44] Q. Sun, O. Gröning, J. Overbeck, O. Braun, M. L. Perrin, G. Borin Barin, M. El Abbassi, K. Eimre, E. Ditler, C. Daniels, V. Meunier, C. A. Pignedoli, M. Calame, R. Fasel, P. Ruffieux, *Adv. Mater.* **2020**, *32*, 1906054.

[45] M. Camarasa-Gomez, D. Hernangomez-Perez, M. S. Inkpen, G. Lovat, E. D. Fung, X. Roy, L. Venkataraman, F. Evers, *Nano Lett.* **2020**, *20*, 6381.

[46] G.-P. Zhang, Y.-Q. Mu, M.-Z. Wei, S. Wang, H. Huang, G.-C. Hu, Z.-L. Li, C.-K. Wang, *J. Mater. Chem. C* **2018**, *6*, 2105.

[47] S. Wang, M.-Z. Wei, G.-C. Hu, C.-K. Wang, G.-P. Zhang, *Org. Electron.* **2017**, *49*, 76.

[48] X. Zhao, G. Kastlunger, R. Stadler, *Phys. Rev. B* **2017**, *96*, 085421.

[49] D. Thompson, C. A. Nijhuis, *Acc. Chem. Res.* **2016**, *49*, 2061.

[50] L. Cao, L. Yuan, M. Yang, N. Nerngchamnong, D. Thompson, X. Yu, D.-C. Qi, C. A. Nijhuis, *Nanoscale Adv.* **2019**, *1*, 1991.

[51] B. Han, Y. Li, X. Ji, X. Song, S. Ding, B. Li, H. Khalid, Y. Zhang, X. Xu, L. Tian, H. Dong, X. Yu, W. Hu, *J. Am. Chem. Soc.* **2020**, *142*, 9708.

[52] C. Jia, I. M. Grace, P. Wang, A. Almeshal, Z. Huang, Y. Wang, P. Chen, L. Wang, J. Zhou, Z. Feng, Z. Zhao, Y. Huang, C. J. Lambert, X. Duan, *Chem.* **2020**, *6*, 1172.

[53] H. Jeong, D. Kim, G. Wang, S. Park, H. Lee, K. Cho, W.-T. Hwang, M.-H. Yoon, Y. H. Jang, H. Song, D. Xiang, T. Lee, *Adv. Funct. Mater.* **2014**, *24*, 2472.

[54] J. J. Henderson, C. M. Ramsey, E. del Barco, A. Mishra, G. Christou, *J. Appl. Phys.* **2007**, *101*, 09E102.

[55] R. Liu, J.-J. Bi, Z. Xie, K. Yin, D. Wang, G.-P. Zhang, D. Xiang, C.-K. Wang, Z.-L. Li, *Phys. Rev. Appl.* **2018**, *9*, 054023.

[56] Q. Wang, R. Liu, D. Xiang, M. Sun, Z. Zhao, L. Sun, T. Mei, P. Wu, H. Liu, X. Guo, Z. L. Li, T. Lee, *ACS Nano* **2016**, *10*, 9695.

[57] H. Song, M. A. Reed, T. Lee, *Adv. Mater.* **2011**, *23*, 1583.

[58] A. Escorcia, A.-A. Dhirani, *J. Electroanal. Chem.* **2007**, *601*, 260.

[59] M. Brandbyge, J.-L. Mozos, P. Ordejón, J. Taylor, K. Stokbro, *Phys. Rev. B* **2002**, *65*, 165401.